The Community Stress-Drop Validation Study—Part I: Source, Propagation, and Site Decomposition of Fourier Spectra

Dino Bindi[*1], Daniele Spallarossa[2], Matteo Picozzi[3], Adrien Oth[4], Paola Morasca[5], and Kevin Mayeda[6]

Abstract

As part of the community stress-drop validation study initiative, we apply a spectral decomposition approach to isolate the source spectra of 556 events occurred during the 2019 Ridgecrest sequence (Southern California). We perform multiple decompositions by introducing alternative choices for some processing and model assumptions, namely: three different *S*-wave window durations (i.e., 5 s, 20 s, and variable between 5 and 20 s); two attenuation models that account differently for depth dependencies; and two different site amplification constraints applied to restore uniqueness of the solution. Seismic moment and corner frequency are estimated for the Brune and Boatwright source models, and an extensive archive including source spectra, site amplifications, attenuation models, and tables with source parameters is disseminated as the main product of the present study. We also compare different approaches to measure the precision of the parameters expressed in terms of 95% confidence intervals (CIs). The CIs estimated from the asymptotic standard errors and from Monte Carlo resampling of the residual distribution show an almost one-to-one correspondence; the approach based on model selection by setting a threshold for misfit chosen with an *F*-ratio test is conservative compared to the approach based on the asymptotic standard errors. The uncertainty analysis is completed in the companion article in which the outcomes from this work are used to compare epistemic uncertainty with precision of the source parameters.

Cite this article as Bindi, D., D. Spallarossa, M. Picozzi, A. Oth, P. Morasca, and K. Mayeda (2023). The Community Stress-Drop Validation Study—Part I: Source, Propagation, and Site Decomposition of Fourier Spectra, *Seismol. Res. Lett.* **94**, 1980–1991, doi: 10.1785/0220230019.

Supplemental Material

Introduction

Determination of source properties of small and moderate earthquakes from far-field recordings requires adequate treatment of propagation and site effects. Over the years, various approaches in the time or spectral domain have been developed to isolate the source contribution in recordings, and to determine parameters such as seismic moment and source size. Examples are deconvolution with an empirical Green's function in time (e.g., Mori and Frankel, 1990; Bertero *et al.*, 1997) or frequency (e.g., Mueller, 1985; Abercrombie, 2015) domain, considering *P*- or *S*-wave windows; coda-envelope decay modeling (e.g., Mayeda *et al.*, 2003; Shelly *et al.*, 2021); and joint inversion of Fourier amplitude spectra (FAS; e.g., Andrews, 1986; Castro *et al.*, 1990). Regardless the approach taken, estimates of source parameter are affected by uncertainties generated by several factors, such as data selection and processing, model assumptions inherent to the inversion schema applied, and adopted fitting procedure. Because of these uncertainties, it is difficult to compare results obtained from different studies, and interpretation of source-scaling relationships and spatial variability is hampered by the various study-dependent assumptions (Abercrombie, 2021).

Recently, benchmark studies have been carried out to facilitate comparison of the results of different approaches applied to the same data set (e.g., Shearer *et al.*, 2019; Baltay *et al.*, 2021; Pennington *et al.*, 2021; Morasca *et al.*, 2022; Shible *et al.*, 2022). In this study, we consider the data set disseminated in the context of the community stress-drop validation study (see Data and Resources) organized to compare the source parameters and, in particular, stress drop for earthquakes of

1. German Research Centre for Geoscience GFZ, Potsdam, Germany, https://orcid.org/0000-0002-8619-2220 (DB); 2. Department for Earth, Environment and Life Sciences DISTAV, University of Genova, Genova, Italy, https://orcid.org/0000-0002-8021-3908 (DS); 3. Department of Physics, University of Naples Federico II, Naples, Italy, https://orcid.org/0000-0001-8078-9416 (MP); 4. European Center for Geodynamics and Seismology, Walferdange, Grand-Duchy of Luxembourg, https://orcid.org/0000-0003-4859-6504 (AO); 5. National Institute of Geophysics and Volcanology INGV, Milan, Italy, https://orcid.org/0000-0002-6525-4867 (PM); 6. Air Force Technical Applications Center AFTAC, Patrick Air Force Base, Florida, U.S.A., https://orcid.org/0000-0003-0980-0605 (KM)

*Corresponding author: bindi@gfz-potsdam.de

the 2019 Ridgecrest sequence in Southern California. We consider a spectral decomposition approach known as generalized inversion technique (GIT; Oth *et al.*, 2011) to determine the nonparameteric source spectra of the analyzed earthquakes. Because our focus is on estimating the uncertainties on the source parameters, we carry out the spectral decomposition by performing alternative assumptions for different components of the workflow (i.e., window duration for Fourier computation, dependency on depth of attenuation model, applied site amplification constraint, and assumed source model). In fact, this article is the first of a two-part study (see Data and Resources). Here, we provide an overview of the decomposition performed, focusing on evaluating the uncertainty of the parameters associated with the spectral fitting procedure, hereafter referred to as the precision of the source parameters; in the companion article (see Data and Resources), the uncertainty sampled from the multiple choices (model-related or epistemic uncertainty) is estimated and compared with the precision. As the main product of the present study, an archive is available that includes source spectra, tables listing the source parameters obtained for the alternative choices, and figures showing the performed fits (see Appendix for details about the archive).

Data Set

Recordings analyzed in this study are extracted from the data set disseminated in the framework of the community stress-drop validation study (Baltay *et al.*, 2021). We consider 556 earthquakes recorded at 67 sites, corresponding to 94 stations if colocated sensors are counted separately. We analyze accelerometric (HN or HL) and velocity (HH or EH) data channels provided by different networks (see Data and Resources). Local or moment magnitudes M are in the range 2.5–7.1, hypocentral distances cover the range 5–111.4 km, and the hypocentral depths are shallower than 12 km. The source-to-station geometry of the data set is shown in Figure 1. FAS are computed for three different windows durations, starting one second before the *S*-wave arrival time. The selected durations are 5 s, 20 s, and a variable duration ending when the squared velocity cumulated over the entire window reaches 90%. In the latter case, we limit the minimum and the maximum durations to 5 and 20 s, respectively. The minimum and the maximum durations are selected to have a good spectral resolution at 0.3 Hz (i.e., the lowest frequency considered for the source spectra) and to avoid long coda durations for the largest distances analyzed, respectively. A comparison of the FAS computed for 5 and 20 s windows is shown in Figure S1, available in the supplemental material to this article, for two events with magnitude 2.7 and 5.4, respectively, considering recordings at different hypocentral distances. Beside the difference in spectral resolution, deviations between the spectra computed considering the two durations are observed at low frequencies, in particular, for the short distance (11.7 km) recording of the

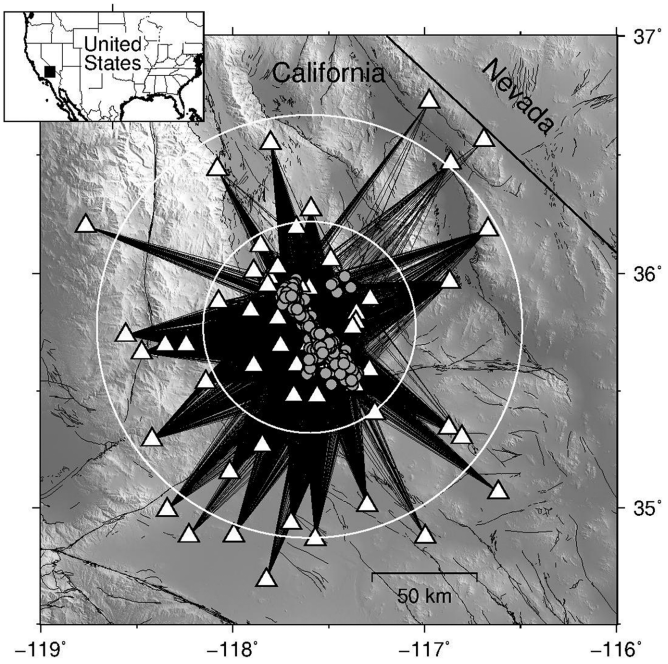

Figure 1. Map of the Ridgecrest region (Southern California) showing the locations of events (circles) and stations (triangles) considered in this study. Rays are connecting epicenters to recording stations. The circles with radius 50 and 100 km are drawn for reference.

M 2.7 event and for the recordings of the M 5.4 event at 34.7 and 100 km. Therefore, an impact of the window duration on the estimate of the seismic moment is expected (see companion article in the Data and Resources section). The acceleration FAS are smoothed using the Konno–Ohmachi window with $b = 40$ (Konno and Ohmachi, 1998), and the two horizontal spectra are vectorially combined. Signal-to-noise ratio (SNR) is evaluated considering pre-event noise windows and retaining for analysis only those spectral amplitudes with SNR greater than 4, discarding spectra with less than 60% of usable frequencies. The maximum number of spectral amplitude available for the analysis is 11,102 at 2.23 Hz; the spectral amplitudes are reduced to 7731 and to 6553 at 0.3 and 30 Hz, respectively. Finally, only stations and events with at least eight usable recordings are retained for the analysis.

Spectral Decomposition

The so-called GIT is a well-established approach to isolate source, propagation, and site effects in the spectral domain (Andrews, 1986; Castro *et al.*, 1990; Boatwright *et al.*, 1991; Oth *et al.*, 2011). GIT is based on linear and time-invariant assumptions for which the output is given by the convolution between the input and the transfer function of the system, that is

$$\mathrm{Log}O_{ij}(f) = \mathrm{Log}S_i(f) + \mathrm{Log}P(R_{ij},f) + \mathrm{Log}Z_j(f), \quad (1)$$

in which the $O_{ij}(f)$ is the observed spectral amplitude at frequency f for earthquake i recorded at station j; $S_i(f)$ is the source spectrum for event i; $P(R_{ij},f)$ is the propagation term for the hypocentral distance R_{ij}; and $Z_j(f)$ is the site term for station j. Considering each frequency separately, equation (1) is generating an overdetermined linear system that can be solved in a least-squares sense. Then, the results achieved for the different frequencies are merged to form vectors describing the source spectrum for each considered earthquake—the spectral attenuation with distance and site effects for all stations. The nonparametric source spectra can be fit at a later stage to any suitable seismological model to extract the source parameters of interest.

We consider two alternative approaches for describing the propagation term P. In the first approach, P is described in terms of the spectral attenuation with hypocentral distance A^R; following this approach, the attenuation for two source-to-receivers seismic rays corresponding to the same hypocentral distance, but starting at different hypocentral depths is the same. To introduce an explicit dependence on the source depth, a set of spectral attenuation models A^{rh} are simultaneously determined for different depth interval, considering the epicentral distance. The two nonparametric propagation models are described by the following equations:

$$\mathrm{Log}P_{ij}(f_k) = a_n(f_k)\mathrm{Log}A^R_n + a_{n+1}(f_k)\mathrm{Log}A^R_{n+1}, \tag{2}$$

$$\begin{aligned}\mathrm{Log}P_{ij}(f_k) = {} & b_{m,l}(f_k)\mathrm{Log}A^{rh}_{m,l} + b_{m+1,l}(f_k)\mathrm{Log}A^{rh}_{m+1,l} \\ & + b_{m,l+1}(f_k)\mathrm{Log}A^{rh}_{m,l+1} \\ & + b_{m+1,l+1}(f_k)\mathrm{Log}A^{rh}_{m+1,l+1}.\end{aligned} \tag{3}$$

In the following, we refer to models in equations (2) and (3) as hypocentral distance-based model (HYPO) and depth-dependent models for epicentral distance (EPIH) models, respectively.

For HYPO, we discretize the analyzed hypocentral distance range into N intervals with nodes located at distances R_n, with $n = 0,\ldots, N-1$; a linear interpolation of $\mathrm{Log}A^R$ is assumed between two consecutive nodes, that is, if the hypocentral distance R satisfies the condition $R_n \le R < R_{n+1}$, then $a_n = (R_{n+1} - R)/\Delta R$ and $a_{n+1} = 1 - a_n$ with $\Delta R = (R_{n+1} - R_n)$. For EPIH, both the epicentral and depth ranges are discretized into M and L intervals corresponding to distances r_m, with $m = 0,\ldots, M-1$ and depths h_l, with $l = 0,\ldots, L-1$, respectively. The distance vector used for HYPO is [0, from 5 to 107 with step 3, 111.5] km.

Also, a linear interpolation between consecutive epicentral distances and consecutive depths is implemented for EPIH. The considered depth interfaces are [0, 3, 6, 9, 11.5] km. Therefore, for each frequency, the spectral attenuation with hypocentral distance is represented by a vector of values a_n (HYPO model), whereas the spectral attenuation with epicentral distance and depth is represented by a matrix $b_{m,l}$ of values (EPIH model). To smooth the spectral attenuation values with distance and depth, we set to zero the Laplacian computed with respect to the variables, and we solve the linear system equation (1) in a least-squares sense (Koenker and Ng, 2021).

The HYPO and EPIH models are shown in Figure 2. For distances less than 50 km, HYPO spectral values averaged over different frequency intervals attenuate with distance between $1/R$ (low frequencies) and $1/R^{1.6}$ (high frequencies); for longer distances, high frequencies attenuate more rapidly, whereas low frequencies show a tendency to become flat, probably as a consequence of reflections from deep crustal interfaces (e.g., Somerville and Yoshimura, 1990). The EPIH model is exemplified in Figure 2 for three frequencies: at 1 Hz, attenuation is weak at all depth intervals; at intermediate frequencies (about 4 Hz), attenuation shows a systematic dependency on depth, with shallow depths attenuating more; and at high frequencies (about 15 Hz), depths up to 9 km show a similar trend, whereas attenuation for the two deeper depth ranges is weaker. In summary, Figure 2 shows that the EPIH model shows a tendency for attenuation to decrease with depth with more pronounced differences between the depth ranges occurring at intermediate frequencies. The impact of the selected attenuation model on the source parameters is discussed in the companion article (see Data and Resources).

Nonuniqueness of the GIT Solution

The least-squares solution of system 1 is not unique, because there are two unresolved degrees of freedom: because we are summing three terms, we can add a constant to one term and remove the same constant from another, and the sum will not change (Andrews, 1986). To check the rank deficiency of the design matrix, we perform its singular value decomposition:

$$G = USV^T, \tag{4}$$

in which G is the $M{\times}N$ design matrix; U is the $M{\times}M$ orthogonal matrix for which columns generate the data space; V is the $N{\times}N$ orthogonal matrix for which columns generate the model space; and S is an $M \times N$ diagonal matrix with nonnegative diagonal elements called singular values. The singular values for the geometry of Figure 1 are shown in Figure S2. As expected, among the 687 singular values, two are numerically close to zero (i.e., of the order of 10^{-16}), confirming that the model null space has dimension equal to 2. The right panel of Figure S2 shows the columns $V_{,686}$ and $V_{,687}$ of the matrix V, which are associated with the null singular values (the singular values are organized in descending order). These two columns form an orthonormal basis for the kernel of the design matrix. Each element of the basis consists of a constant value on each column block related to event, station, and attenuation with the sum of the three constant values equal to 0. They represent the

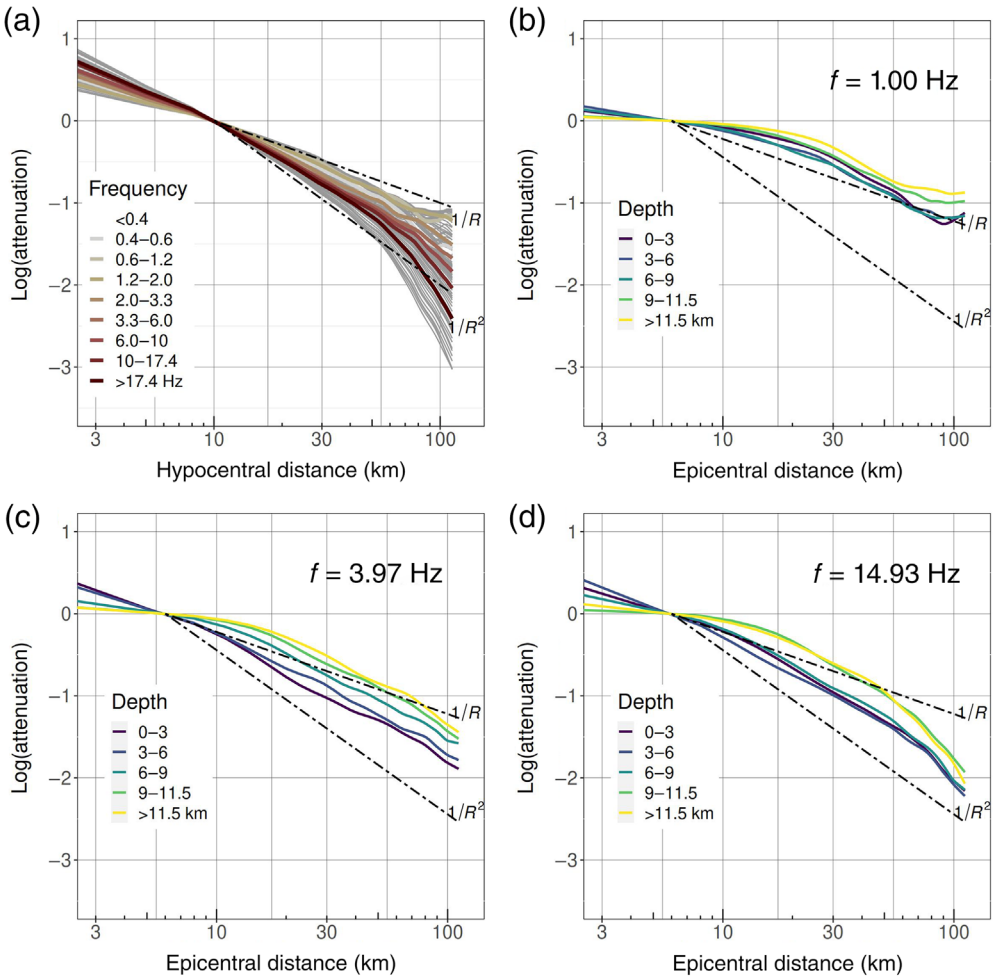

Figure 2. Hypocentral distance (HYPO) and epicentral distance for different depth intervals (EPIH) attenuation models described by equations (2) and (3), respectively. (a) The thin lines represent the HYPO values for different frequencies; the thick colored lines represent the HYPO attenuation values averaged over different frequency intervals as indicated in the legend. (b–d) EPIH attenuation values exemplified for different frequencies (as indicated in each panel); different colors indicate the attenuation values for different depth ranges as indicated in the legend. Attenuation values proportional to $1/R$ and $1/R^2$ (dashed dotted lines) are shown for reference. The color version of this figure is available only in the electronic edition.

tradeoff existing among the source, station, and propagation terms and without additional information (constraints), the solution of the system 1 is not unique.

Other important information associated with the GIT design matrix is provided by the covariance matrix (Boatwright *et al.*, 1991; Bindi *et al.*, 2006). Figure 3a shows the diagonal elements of the covariance matrix, that is, the sample variances of the model parameters. The off-diagonal elements of the covariance matrix provide information about the tradeoffs (correlation) between different model parameters that jointly contribute to generating the observations. These tradeoffs are determined by the geometry of the problem. Figure 3b shows that there is a tradeoff between station and attenuation model parameters. For example, Figure 3c focuses on model parameter 560 corresponding to station WBM (Bowman Road) of the Southern California seismic network (CI). The recordings analyzed for this station are in the distance range of 25–50 km, with median and mode hypocentral distance equal to about 35 km. Figure 3d confirms that there is a tradeoff between the station term and the attenuation coefficients in the distance range sampled by the station, in particular, for the mostly sampled distances. To limit the tradeoffs, it is important that different stations sample the same distance bins, avoiding that a few stations dominate specific distance intervals, and that each station provides recordings over wide distance and magnitude intervals (Shible *et al.*, 2022).

To remove the two null-singular values, the solution is forced to satisfy specific conditions that make the matrix full rank. The first constraint is applied to the attenuation model by assuming a reference distance at which the attenuation is fixed to 1, that is, $\log P_k = 0$ for $R_k = R_{\mathrm{ref}}$. As a consequence, the source spectra are scaled at R_{ref}. We fix the hypocentral and epicentral reference distance for the HYPO and EPIH attenuation models to 10 and 6 km, respectively.

We apply the second constraint to the site amplifications by assuming a reference amplification condition. We consider two different references; the first choice (referred to as AVE) is to constrain to zero the average of the logarithm of all site amplifications at each frequency; the second choice (referred to as SEL) is to set the average site amplification relevant to a set of reference stations equal to the a priori chosen amplification function $Z_{\mathrm{ref}}(f)$.

The site amplifications obtained with the AVE constraint are shown in Figure 4a. Because the considered stations are installed in different geological settings, the site amplifications show a large variability in particular above 10 Hz. The applied constraint implies that the site terms represent the site

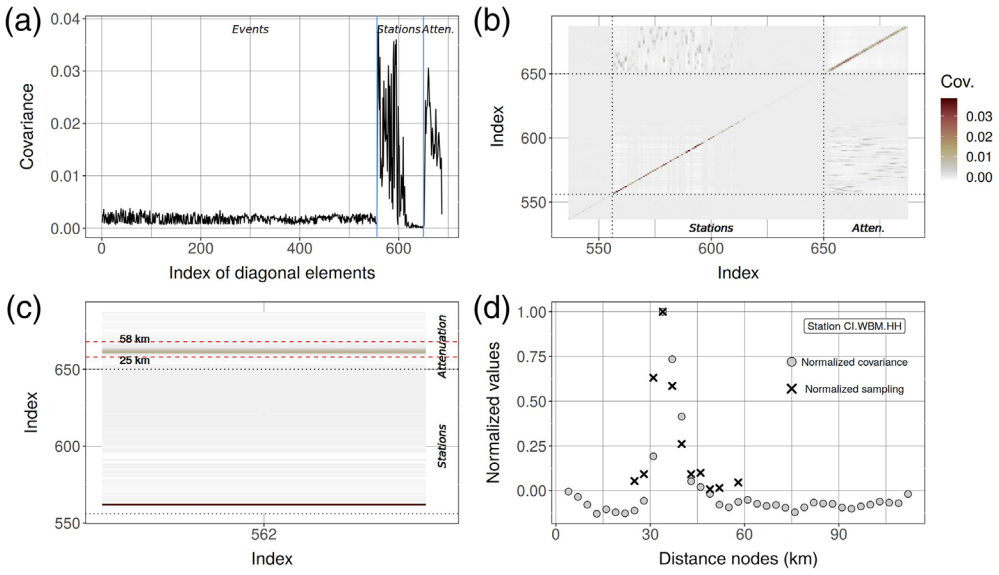

Figure 3. (a) Diagonal elements of the covariance matrix. (b) Detail of the covariance matrix considering the station and attenuation columns. (c) Detail of the covariance matrix for station CI.WBM.HH (column 560) considering only the station and attenuation portion of the matrix. The red dashed lines indicate the distance range sampled by recordings at CI.WBM.HH. (d) The circles indicate the normalized covariance off-diagonal entries between station CI.WBM.HH and the attenuation columns; crosses indicate the number of recordings for station CI.WBM.HH available within each distance bin, normalized to the maximum sampling. The color version of this figure is available only in the electronic edition.

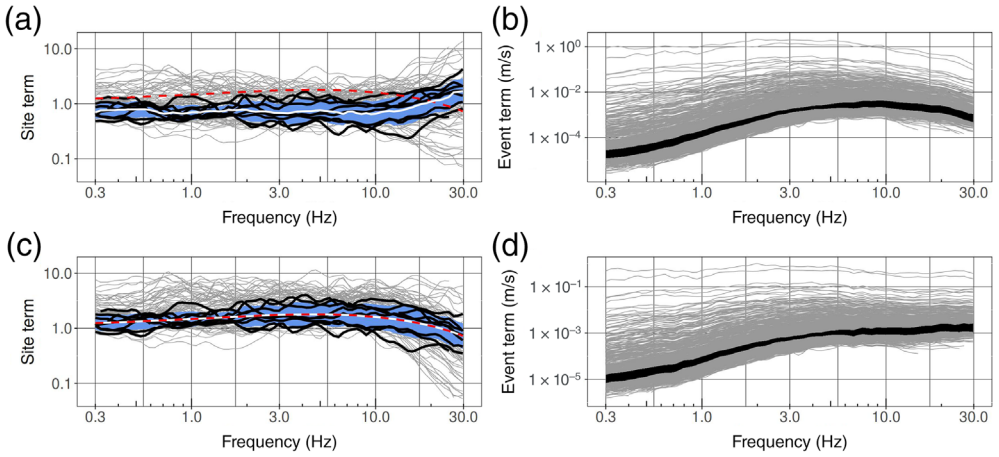

Figure 4. Impact on the source spectra of constraints applied to the site term. (a) Site amplifications obtained by constraining the average of all site terms to 1. (b) Source spectra relevant to the site terms as in panel (a). (c) Site amplifications obtained by constraining the average (white curve) of selected rock sites (black curves) to be identical to the spectral function shown as a dashed line; the same reference sites (black) and their average amplification (white) ± one standard deviation are also shown in panel (a). (d) Source spectra relevant to the site terms in panel (c). In panels (b) and (d), the black curves are source spectra of magnitude 3 events. The color version of this figure is available only in the electronic edition.

amplifications with respect to the network average. If the average amplification deviates from the imposed flat spectral behavior, the deviation from the true average is moved to the source spectra shown in Figure 4b. The acceleration source spectra show an average high-frequency decay different from the flat asymptotic behavior predicted by the omega-square source model, and the absorbed average site amplification contributes to the observed high-frequency spectral fall off. The SEL constraint is applied to the average site amplification of six stations installed on rock (measured or geologically inferred V_{S30} values greater than 710 m/s from Rekoske *et al.*, 2020) shown as black curves in Figure 4a. They have a flat amplification lower than the network average at frequencies smaller than about 10 Hz, and then they show a positive amplification trend with frequency. The positive trend indicates that the near-surface attenuation for these stations (k_0 parameter, Anderson and Hough, 1984) is probably weaker than the average near-surface attenuation of the overall network. Therefore, following (Bindi *et al.*, 2020), we constrain the average amplification of the six stations to the crustal amplification $C(f)$ proposed by (Campbell and Boore, 2016) for the National Earthquake Hazards Reduction Program (NEHRP) B/C boundary multiplied by an exponential term with $k_0 = 0.016$ s (Fig. 4c, dashed line), that is

$$Z_{\mathrm{ref}}(f) = C(f)e^{-\pi k_0 f}. \qquad (5)$$

The values used for k_0 allows to get acceleration source spectra that are, on average, flat at high frequencies (Fig. 4d), as predicted by ω^2 source models. Although the actual source spectra could deviate from this behavior due to near-source attenuation (Castro *et al.*, 2022) or source

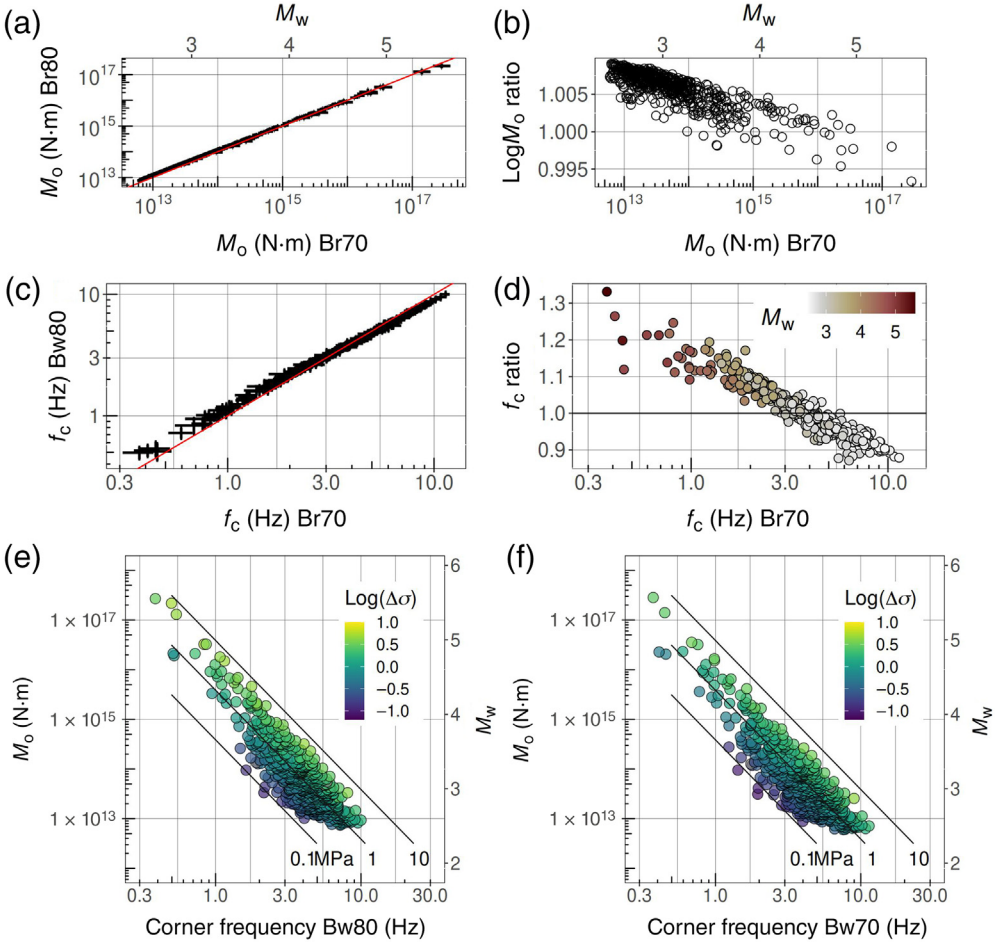

Figure 5. Comparison between the logarithm of seismic moment M_0 and corner frequency f_c estimated considering the Brune (Br70; $n = 1$, $\gamma = 2$ in equation 6) (a) and Boatwright (Bw80; $n = 2$, $\gamma = 2$ in equation 6) (c) source models. Ratios in panels (b) and (d) are computed as Br70/Bw80. Panels (e) and (f) show the scaling between seismic moment and corner frequency for Bw80 and Br70 models, respectively. The color version of this figure is available only in the electronic edition.

In equation (6), the source for each earthquake is characterized by the parameters Ω^0 (proportional to the seismic moment M_0), the corner frequency f_c, and the high-frequency decay parameters n and γ. To reduce the number of source parameters, the latter are sometimes constrained to a priori values corresponding to specific source models. We consider two different choices: $\gamma = 2$ and $n = 1$, corresponding the Brune ω^2 source model (Brune, 1970), and $\gamma = 2$ and $n = 2$, referred to as Boatwright model. Therefore, we fit two different models to the source spectra $S(f)$ to obtain seismic moment M_0 and corner frequency f_c values for the analyzed earthquakes. The source parameters for the Brune and Boatwright models are compared in Figure 5, considering 20 s windows, HYPO attenuation model, and SEL site constraint. Figure 5a,b shows that the seismic moments estimated for the two source models are in good agreement with ratios less than 1%. The trend in Figure 5b is a consequence of the inverse (Beresnev, 2023) effects, with the SEL constraint we impose that the source spectra are ω^2.

If we compare the logarithm of the ratio between the average spectra for magnitude 3 events with the logarithm of the inverse average site amplifications for the reference stations, they are identical (see Fig. S3). This confirms that the constraint applied to the site amplifications breaks the tradeoff between source and site terms, but the constrained solutions provide the same predictions, because the unconstrained solutions and the analysis of the residuals alone is not sufficient to discriminate among the quality of solutions obtained by applying different constraints.

Source Parameters

We fit the GIT source spectra $S(f)$ to the following rupture source model (Boatwright, 1980):

$$S(f) = \frac{\Omega^0}{[1 + (f/f_c)^{n\gamma}]^{1/n}}. \quad (6)$$

Regarding the corner frequencies, Figure 5c,d show that there is a systematic scaling between the values of f_c provided by the two source models, with the ratio of the Boatwright to Brune values showing a trend with negative slope as f_c increases (i.e., as magnitude decreases). The seismic moment versus corner frequency scaling are shown in Figure 5e,f and compared with the equal stress drop lines (Hanks and Thatcher, 1972; Thatcher, 1972). The computation of the stress drop is described in the companion article (see Data and Resources). Despite differences in individual values, the overall population of events considered show a similar scaling for the two source models, with stress drops mostly between 0.1 and 10 MPa. Although the maximum stress-drop value shown by events of different magnitude is almost independent of magnitude, smaller events show larger variability toward small values of stress drop.

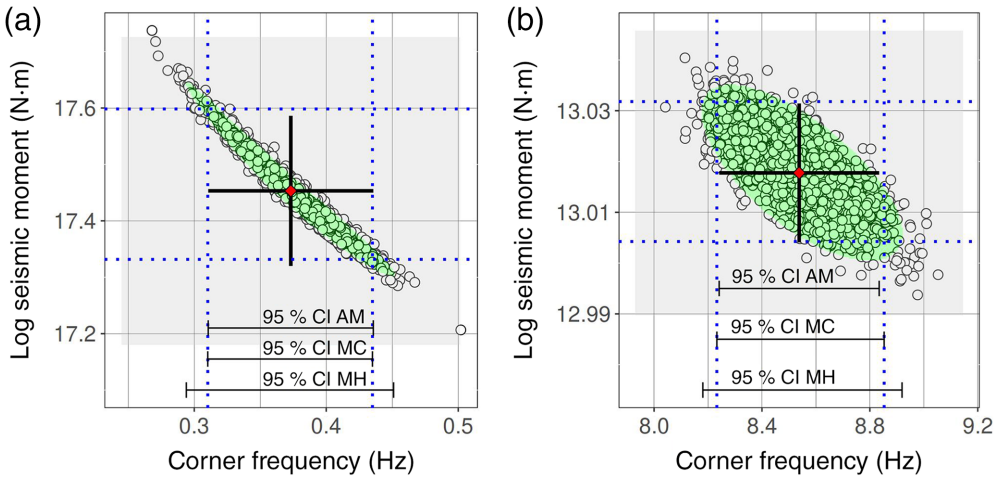

Figure 6. Confidence intervals computed with different methods for two events with magnitude (a) 5.4 and (b) 2.7. The considered methods are based on: asymptotic standard error (AM); Monte Carlo resampling of the residual distribution (MC); and model comparison (MH). The diamond in the center indicates the best-fit parameters with the AM confidence intervals (horizontal and vertical black segments); the circles represent the Monte Carlo solutions with their 95% confidence intervals (horizontal and vertical dotted lines); the large gray square indicates the grid search domain explored for the model comparison approach MH, and the ellipsoid over the Monte Carlo results delimits the 95% confidence contour for MH. The color version of this figure is available only in the electronic edition.

Regarding the AVE site constraint because an average site effects could be transferred to the source term, equation (6) is modified as

$$S(f) = \frac{\Omega^0}{[1 + (f/f_c)^{n\gamma}]^{1/n}} e^{-\pi(f-f_s)k_s}, \quad (7)$$

in which the additional factor, applied for $f \geq f_s$, accounts for deviations of the high-frequency trend from a flat acceleration spectra. The average of the k_s slopes computed over the source population is linked to the average site k_0 transferred to the source terms by the AVE constraint, whereas event-specific deviations from the average represent source-specific effects (Bindi *et al.*, 2020). For each spectrum, the value of f_s in equation (7) is determined by following a grid search procedure. Finally, the source spectra are anchored to the catalog moment magnitudes by requiring that the average of the seismic moments M_0 estimated from Ω^0 do not show any bias with respect to the catalog values for events with magnitude larger than 3.5 (see Bindi *et al.*, 2020, their equation 4).

Precision of the Source Parameters

The source parameters are provided with 95% confidence intervals (CIs). Because different approaches can be applied to compute the CI (Motulsky and Christopoulos, 2004), we compare three procedures based on asymptotic standard errors (method AM), Monte Carlo resampling (method MC), and model comparison (method MH).

In the AM approach, the 95% CI of the best-fit parameter p (in which p indicates either $\mathrm{Log}M_0$ or f_c) is computed as $p \pm t_{\alpha,df}\mathrm{SE}$, in which t is the t-student critical value for the selected confidence level (i.e., $\alpha = (1 - 0.95)/2$) and the number of degrees of freedom df. The standard error (SE) of the parameters is extracted from the diagonal of elements of the covariance matrix. Figure 6 exemplifies the width of the confidence intervals computed for two earthquakes of magnitude 5.4 (Fig. 6a) and 2.7 (Fig. 6b), considering the Brune model. Results are relevant to the decomposition applied considering the HYPO attenuation model and the SEL constraint on site amplifications. The best fit f_c and $\mathrm{Log}M_0$ parameters are indicated by the diamond, and the crosses indicate the extension of the AM estimates for the 95% CI of the best-fit parameters.

In the MC approach, spectra generated by considering the best-fit parameters are perturbed with random scatter and fitted again. A large number of random scatter realizations (2000 in our case) are drawn from a Gaussian distribution with zero mean and standard deviation equal to the standard deviation of the residual distribution associated to the best-fit model. Then, a distribution of source parameters is generated for all synthetic spectra, and the range between the 2.5th and 97.5th percentile values are used as MC estimate of the confidence intervals. In Figure 6, the best-fit models of the 2000 Monte Carlo randomly generated spectra are shown as circles, and the MC confidence intervals for f_c and $\mathrm{Log}M_0$ are indicated by the dashed lines. The Monte Carlo approach provides also a visual indication about the correlation between the two source parameters, which is stronger for the larger event shown in Figure 6a. A larger correlation for the magnitude 5.4 event is also confirmed by the correlation coefficients computed by normalizing the off-diagonal element of the covariance matrix for the standard deviation of the two parameters (the correlation coefficients are −0.65 and −0.95 for the 2.7 and 5.4 events, respectively), and it was expected because its corner frequency is close to the lower boundary of the usable frequency range (i.e., 0.3 Hz).

The MH confidence intervals are constructed selecting models that produce errors smaller than a threshold fixed

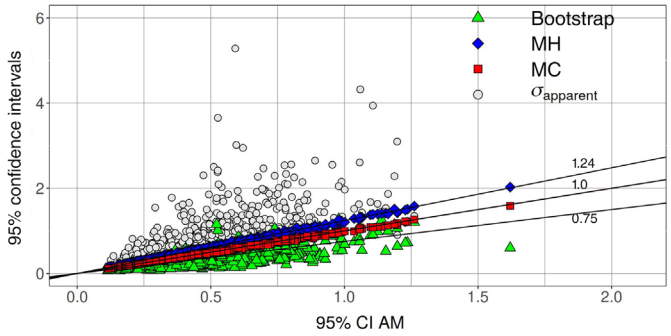

Figure 7. Confidence interval of f_c computed with different approaches versus the values provided by approach AM based on asymptotic standard error. Bootstrap results are shown as triangles, and the points represent the results for the apparent corner frequencies. The color version of this figure is available only in the electronic edition.

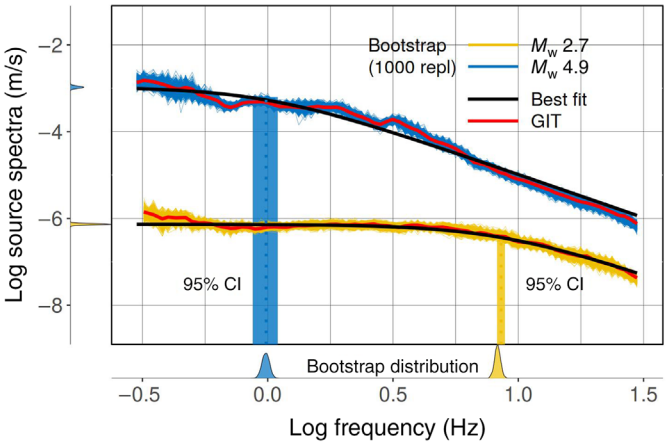

Figure 8. Results of the bootstrap analysis exemplified for two events of magnitude 2.7 and 5.4. The 95% CI on f_c for the best-fit model estimated with the AM method are shown as vertical strips; the bell-shaped distributions are the distributions of the source parameters estimated by fitting the Brune model to the bootstrap spectra (1000 replications). The color version of this figure is available only in the electronic edition.

above the minimum misfit value. The misfit is measured in terms of sum-of-squares (SS), and the threshold is selected such that models with SS below the threshold cannot be considered statistically different from the best-fit model by performing an F-ratio test at 95% confidence level. The value of the threshold is given by (Motulsky and Christopoulos, 2004):

$$SS_{threshold} = SS_{best-fit}\left(F\frac{P}{N-P}+1\right), \quad (8)$$

in which $SS_{best-fit}$ is the sum-of-squares value of the best-fit model, P is the number of model parameters (2 in our case), N is the number of spectral values, and F is the critical value of the F distribution for $1-\alpha = 0.05$ confidence level with P degrees-of-freedom in the numerator and $N-P$ in the denominator. A grid search procedure is implemented to identity those models generating a SS not larger than $SS_{threshold}$. In Figure 6, the tested models are those within the large rectangular domain, and models with SS below the threshold define the ellipsoid within the grid search area. The MH confidence intervals are computed considering the lowest and the highest values of the parameters on the boundary of the ellipsoid (confidence contour). Figure 6 shows that the MH confidence intervals for f_c and LogM_0 are conservative with respect to AM and MC estimates. The comparison between the different estimates CI for f_c is shown in Figure 7, considering all the events. AM and MC produce almost identical estimated (squares on the line with slope 1), whereas MH generates CI for f_c about 25% larger (diamonds on the line with slope 1.24). Because the different approaches produce consistent estimates, in the following we consider the AM confidence intervals for their lower computational effort requirement.

Following the previous studies (Prieto *et al.*, 2007; Oth *et al.*, 2011), we also consider the nonparametric bootstrap approach (Efron, 1979) to estimate the uncertainties of the source parameters. The bootstrap procedure is applied to the input data set by randomly sampling with repetition the original data set and creating 1000 replications. The GIT decomposition is performed for each replication, and a distribution of spectra is obtained for each event. Figure 8 shows the bootstrap spectra distribution for two events with magnitude 2.7 and 5.4, being the GIT source spectra estimated from the original data set close to the median of the bootstrap spectral distribution. A distribution of source parameters is then generated by fitting the Brune source model to each bootstrap spectrum, and the % 95 CI for the parameters is computed as difference between the 2.5th and 97.5th percentiles. Figure 8 shows that the corner frequency bootstrap distributions (bell-shaped distributions on the bottom line) have a similar extension as the %95 CI for the corner frequency estimated from the GIT results of the original data set (vertical ribbon). When applied to all earthquakes, the estimated bootstrap %95 CI scale linearly with the AS estimate, but with a slope of about 0.75, suggesting that the bootstrap approach overestimates the parameter's precision (i.e., underestimate the uncertainty) with respect the AM, MC, and MH approaches (Fig. 7).

Discussion

Source parameters can be determined by time or frequency analysis after removing or mitigating, propagation, and site effects. In this work, we applied the GIT approach that simultaneously inverts a large set of FAS computed for several earthquakes recorded from a network of stations. By solving an overdetermined linear system in the least-squares sense, a generic source spectrum is isolated for each earthquake from

the spectral attenuation with distance- and site-dependent amplification effects. The generic GIT source spectra are, in turn, fitted to standard omega-square models to compute seismic moments and corner frequencies. We applied the GIT approach to a data set that was compiled for the 2019 Ridgecrest seismic sequence (Southern California) and disseminated in the context of the stress-drop benchmark (Baltay *et al.*, 2021).

The objective of the benchmark is to compare the source parameters and, in particular, the stress drop estimated by different techniques applied to the same data set. The comparison of source parameters is hampered by several factors such as the nonuniqueness of the solution, the different a priori assumptions applied to restore the uniqueness, and the different assumptions behind the considered source model. The nonuniqueness of the solution is an inherent feature of the model used to link source, propagation, and site effects to observations (equation 1), because the design matrix always has 2 null-singular values regardless of the number and quality of data (see Fig. S2). To restore uniqueness, we introduced a reference site constraint (Fig. 4a,b) that fixes the scale and shape of the site amplification. As a result, the GIT site amplifications are relative to this assumption and the source spectra scale accordingly (Fig. 4c,d). Because different strategies can be applied to source or site terms to break the tradeoff, comparison of results provided by different studies should consider relative quantities to remove the effect of a priori assumptions. It is worth noting that the applied constraints generate solutions that fit the data equally well, and thus the analysis of the residuals does not allow us to distinguish the goodness of models relevant to different constraints. Beside the tradeoff among the source, propagation, and site term generated by the two unresolved degrees of freedom, the different terms also show some degree of correlation, since different source, propagation, or site mechanisms can generate similar spectral amplitudes. For example, we exemplified the inverse correlation between site amplifications and attenuation at distances sampled from the recordings of a selected station for the selected Ridgecrest data set. The correlation between competing physical parameters can be quantified by normalizing the corresponding off-diagonal element of the covariance matrix for the standard deviations of the parameters (Fig. 3). Therefore, the covariance matrix provides some hints about the suitability of the data set for performing the GIT analysis.

The target of this study was actually twofold. First, to set up the GIT decomposition by making alternative choices for decisions regarding the window length for spectra calculation, depth dependence of the attenuation model, site constraint, and source models. The results of the GIT inversions performed considering the various branches of the logic defined by the alternative choices earlier are presented in the companion article (see Data and Resources) that discusses the epistemic uncertainties. The second objective of this study was to estimate the uncertainty affecting the seismic moment and corner frequency resulting from spectral fitting. The uncertainty of parameters is also needed to compare results obtained in different studies, and we quantified the precision by computing the 95% CI. We showed that %95 CI computed from the asymptotic standard errors (i.e., using information extracted from the covariance matrix) and running multiple fits over Monte Carlo-simulated source spectra are very close, whereas the approach based on model comparison (i.e., comparing models that produce sum of the squares misfit values within *F*-ratio test-selected threshold with respect to the best-fit model) is conservative, producing on average %95 CI on corner frequency 25% larger (Fig. 7). We also apply the bootstrap approach to the original data set, performing the GIT inversion over 1000 bootstrapped replications. In agreement with the previous studies (e.g., Morasca *et al.*, 2022), the GIT results obtained considering the original data set is close to the median of the bootstrap distribution of source spectra. The CIs for the source parameters computed from the distribution composed by the values extracted from the bootstrap results are on average about 25% lower than the estimates from the asymptotic standard errors (Fig. 7). The comparison of the precision of the source parameters and the epistemic uncertainty associated to alternative model assumptions is discussed in the companion article (see Data and Resources).

The interpretation of the GIT source spectra is based on several assumptions. In particular, the generic source spectra are assumed to represent azimuthally averaged information. In reality, the finite number of observations and their unbalanced azimuthal distribution may introduce systematic deviations from the expected average values (e.g., radiation pattern effects, rupture directivity effects, etc). Therefore, it is also worthwhile to examine the variability of the source parameters computed by fitting the Brune model to the apparent source spectra, that is, the recorded spectra corrected for the GIT attenuation model and site amplification effects. Figure 9 shows the example for two events of magnitude 3.6 (Fig. 9a) and 5.4 (Fig. 9b). Each circle represents the station-dependent seismic moment and corner frequency extracted from the apparent source spectrum. The inverse correlation between the two source parameters is highlighted by the trend line, and it is stronger for the larger event, as indicated by the slope written in top right corner, in agreement with the previous discussions about Figure 6. For these two events, the distribution of the source parameter values do not show any systematic dependency on source-to-station azimuth, and the 95% CI are represented by the horizontal and vertical segments centered on the mean parameter values. When computed for all the events, the obtained standard deviations of the apparent f_c population for each event are compared in Figure 7 to the AM precision. The CI values and the standard deviation considered have different meanings because they relate to different quantities (precision of the mean estimate with respect to the variability of a population of parameters), and larger values of σ are expected. Nevertheless, the

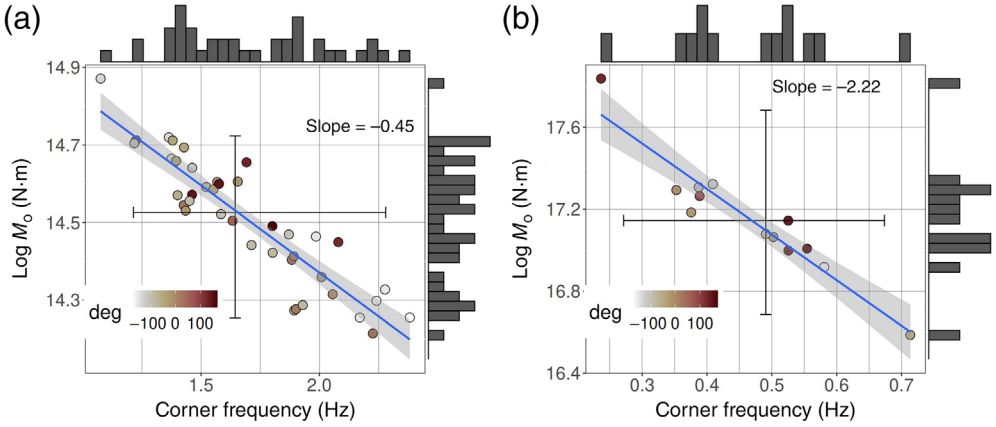

Figure 9. Results on apparent source parameters for two events (each circle is a station that recorded the event) with magnitude (a) 3.6 and (b) 5.4. The color version of this figure is available only in the electronic edition.

comparison in Figure 7 is useful to highlight that the uncertainty on the mean source parameters provides only an estimate of their precision but does not provide any insight about how close they are to the unknown true values, as discussed in the companion article (see Data and Resources).

The results of the analysis (source spectra, attenuation models, site amplifications, and tables of source parameters) are available as products of this study (see Data and Resources). A description of the structure of the archive is provided in the Appendix.

Conclusions

We applied a spectral decomposition approach (GIT) to isolate the source spectra from attenuation and site amplification contributions, considering a data set recorded during the 2019 Ridgecrest sequence (Southern California). In particular:

1. alternative choices for window duration, for describing the distance dependence of the propagation, for constraining the site amplification, and for parametrizing the source spectra have been introduced, computing the seismic moment and corner frequencies for several combinations of these alternative choices;
2. different approaches to estimate the confidence intervals for the seismic moment and corner frequency have been compared. They are based on: asymptotic standard errors extracted from the covariance matrix; simulation based on the Monte Carlo sampling of the residual distribution; model comparison; and bootstrap. The different approaches provide consistent confidence intervals for the source parameters, being the intervals provided by the model comparison approach conservative with respect to the Monte Carlo and asymptotic standard errors approaches. On the other hand, bootstrap estimates are on average about 25% smaller that the Monte Carlo ones; and
3. source parameters have been estimated from the apparent source spectra obtained by correcting the observed spectra for propagation and site effects as provided by GIT, allowing the effectiveness of the azimuth averaging operation to be evaluated.

The parameters produced by combining the alternative choices presented in this article are analyzed in a companion article (see Data and Resources) to compare the precision of the parameters determined in this study with epistemic uncertainties sampled by the multiple choices.

Data and Resources

This study has been performed within the framework of the community stress-drop validation study (Baltay *et al.*, 2021) organized as Southern California Earthquake Center (SCEC) Technical Activity Group. Waveforms and metadata can be available at https://www.scec.org/research/stress-drop-validation. Data from the following seismic networks have been analyzed: CI (doi: 10.7914/SN/CI), GS (doi: 10.7914/SN/GS), SN (doi: 10.7914/SN/SN), NN (doi: 10.7914/SN/NN), PB (not registered), and ZY_1990 (not registered). Analyses have been performed in R (R Core Team, 2020) using packages: ggplot2 (Wickham, 2016), Matrix (Bates *et al.*, 2022), SpareM (Koenker and Ng, 2021), scico (Pedersen and Crameri, 2021), and sparsesvd (Rohde *et al.*, 2019). Figure 1 has been drawn with Generic Mapping Tools software (Wessel *et al.*, 2013). Fault traces in Figure 1 were taken from (Evans *et al.*, 2020), disseminated by SCEC and are available at https://www.scec.org/research/cfm. All websites were last accessed in December 2022. This study is the first of two-article series (Bindi *et al.*, 2023b). The archive with the results of all analyses are available at Bindi *et al.* (2023a). The supplemental material includes Figures S1–S3: Figure S1 shows examples of Fourier amplitude spectra (FAS) computed for different window duration; Figure S2 shows singular values; and Figure S3 shows impact on source spectra of the constraint applied to the site term.

Declaration of Competing Interests

The authors acknowledge that there are no conflicts of interest recorded.

Acknowledgments

The authors thank R. Abercrombie, A. Baltay, and Taka'aki Taira for organizing and managing the community stress-drop validation study. Thanks are also due to three anonymous reviewers and the Associate Editor for providing several useful suggestions. This research has been financially supported by the European Plate

Observing System (EPOS) Research Infrastructure through the contribution of the Italian Ministry of University and Research (MUR)-EPOS ITALIA Joint Research Unit.

References

Abercrombie, R. E. (2015). Investigating uncertainties in empirical Green's function analysis of earthquake source parameters, *J. Geophys. Res.* **120,** no. 6, 4263–4277.

Abercrombie, R. E. (2021). Resolution and uncertainties in estimates of earthquake stress drop and energy release, *Phil. Trans. Roy. Soc. Lond. A* **379,** no. 2196, doi: 10.1098/rsta.2020.0131.

Anderson, J. G., and S. E. Hough (1984). A model for the shape of the Fourier amplitude spectrum of acceleration at high frequencies, *Bull. Seismol. Soc. Am.* **74,** no. 5, 1969–1993.

Andrews, D. J. (1986). Objective determination of source parameters and similarity of earthquakes of different size, in *Earthquake Source Mechanics*, S. Das, J. Boatwright, and C. H. Scholz (Editors), Geophysical Monograph Series, 259–267, doi: 10.1029/GM037p0259.

Baltay, A., R. Abercrombie, and T. Taira (2021). A community stress drop validation study using the 2019 Ridgecrest earthquake dataset, *SSA Annual Meeting*, virtual meeting, 19–23 April 2021.

Bates, D., M. Maechler, and M. Jagan (2022). Matrix: Sparse and dense matrix classes and methods, *R package version 1.4-1*, https://CRAN.R-project.org/package=Matrix (last accessed December 2022).

Beresnev, I. A. (2023). A method to simulate high-frequency decay of acceleration spectra of ground motions without the need for kappa or fmax filters, *Bull. Seismol. Soc. Am.* doi: 10.1785/0120220232.

Bertero, M., D. Bindi, P. Boccacci, M. Cattaneo, C. Eva, and V. Lanza (1997). Application of the projected Landweber method to the estimation of the source time function in seismology, *Inverse Prob.* **13,** no. 2, 465–486.

Bindi, D., S. Parolai, H. Grosser, C. Milkereit, and S. Karakisa (2006). Crustal attenuation characteristics in northwestern turkey in the range from 1 to 10 Hz, *Bull. Seismol. Soc. Am.* **96,** no. 1, 200–214.

Bindi, D., D. Spallarossa, M. Picozzi, A. Oth, P. Morasca, and K. Mayeda (2023a). Spectral decomposition results for the SCEC-community stress drop validation study, *GFZ Data Services* doi: 10.5880/GFZ.2.6.2023.005.

Bindi, D., D. Spallarossa, M. Picozzi, A. Oth, P. Morasca, and K. Mayeda (2023b). The community stress-drop validation study—Part II: Uncertainties of the source parameters and stress drop analysis, *Seismol. Res. Lett.* doi: 10.1785/0220230020.

Bindi, D., R. Zaccarelli, and S. R. Kotha (2020). Local and moment magnitude analysis in the Ridgecrest region, California: Impact on interevent ground-motion variability, *Bull. Seismol. Soc. Am.* **111,** no. 1, 339–355.

Boatwright, J. (1980). A spectral theory for circular seismic sources; simple estimates of source dimension, dynamic stress drop, and radiated seismic energy, *Bull. Seismol. Soc. Am.* **70,** no. 1, 1–27.

Boatwright, J., J. B. Fletcher, and T. E. Fumal (1991). A general inversion scheme for source, site, and propagation characteristics using multiply recorded sets of moderate-sized earthquakes, *Bull. Seismol. Soc. Am.* **81,** no. 5, 1754–1782.

Brune, J. N. (1970). Tectonic stress and the spectra of seismic shear waves from earthquakes, *J. Geophys. Res.* **75,** no. 26, 4997–5009.

Campbell, K. W., and D. M. Boore (2016). Evaluation of six NEHRP B/C crustal amplification models proposed for use in western North America, *Bull. Seismol. Soc. Am.* **106,** no. 2, 673–686.

Castro, R. R., J. G. Anderson, and S. K. Singh (1990). Site response, attenuation and source spectra of S waves along the Guerrero, Mexico, subduction zone, *Bull. Seismol. Soc. Am.* **80,** no. 6A, 1481–1503.

Castro, R. R., L. Colavitti, C. A. Vidales-Basurto, F. Pacor, S. Sgobba, and G. Lanzano (2022). Near-source attenuation and spatial variability of the spectral decay parameter kappa in central Italy, *Seismol. Res. Lett.* **93,** no. 4, 2299–2310.

Efron, B. (1979). Bootstrap methods, another look at the jackknife, *Ann. Stat.* **7,** 1–26.

Evans, W. S., A. Plesch, J. H. Shaw, N. L. Pillai, E. Yu, M. Meier, and E. Hauksson (2020). A statistical method for associating earthquakes with their source faults in southern California, *Bull. Seismol. Soc. Am.* **110,** no. 1, 213–225.

Hanks, T. C., and W. Thatcher (1972). A graphical representation of seismic source parameters, *J. Geophys. Res.* **77,** no. 23, 4393–4405.

Koenker, R., and P. Ng (2021). SparseM: Sparse linear algebra, *R package version 1.81*, https://CRAN.R-project.org/package=SparseM (last accessed December 2022).

Konno, K., and T. Ohmachi (1998). Ground-motion characteristics estimated from spectral ratio between horizontal and vertical components of microtremor, *Bull. Seismol. Soc. Am.* **88,** no. 1, 228–241.

Mayeda, K., A. Hofstetter, J. L. O'Boyle, and W. R. Walter (2003). Stable and transportable regional magnitudes based on coda-derived moment-rate spectra, *Bull. Seismol. Soc. Am.* **93,** no. 1, 224–239.

Morasca, P., D. Bindi, K. Mayeda, J. Roman-Nieves, J. Barno, W. R. Walter, and D. Spallarossa (2022). Source scaling comparison and validation in central Italy: Data intensive direct s waves versus the sparse data coda envelope methodology, *Geophys. J. Int.* **231,** 1573–1590.

Mori, J., and A. Frankel (1990). Source parameters for small events associated with the 1986 North Palm Springs, California, earthquake determined using empirical green functions, *Bull. Seismol. Soc. Am.* **80,** no. 2, 278–295.

Motulsky, H. J., and A. Christopoulos (2004). Fitting models to biological data using linear and nonlinear regression, in *A Practical Guide to Curve Fitting*, GraphPadSoftware Inc., San Diego, California.

Mueller, C. S. (1985). Source pulse enhancement by deconvolution of an empirical green's function, *Geophys. Res. Lett.* **12,** no. 1, 33–36.

Oth, A., D. Bindi, S. Parolai, and D. Di Giacomo (2011). Spectral analysis of K-NET and KiK-net data in Japan, Part II: On attenuation characteristics, source spectra, and site response of borehole and surface stations, *Bull. Seismol. Soc. Am.* **101,** no. 2, 667–687.

Pedersen, T. L., and F. Crameri (2021). scico: Colour palettes based on the scientific colour-maps, *R package version 1.3.0*, https://CRAN.R-project.org/package=scico (last accessed December 2022).

Pennington, C. N., X. Chen, R. E. Abercrombie, and Q. Wu (2021). Cross validation of stress drop estimates and interpretations for the 2011 Prague, ok, earthquake sequence using multiple methods, *J. Geophys. Res.* **126,** no. 3, e2020JB020888, doi: 10.1029/2020JB020888.

Prieto, G. A., D. J. Thomson, F. L. Vernon, P. M. Shearer, and R. L. Parker (2007). Confidence intervals for earthquake source parameters, *Geophys. J. Int.* **168,** no. 3, 1227–1234.

R Core Team (2020). R: A language and environment for statistical computing, R Foundation for Statistical Computing, Vienna, Austria.

Rekoske, J. M., E. M. Thompson, M. P. Moschetti, M. G. Hearne, B. T. Aagaard, and G. A. Parker (2020). The 2019 Ridgecrest, California, earthquake sequence ground motions: Processed records and derived intensity metrics, *Seismol. Res. Lett.* **91,** no. 4, 2010–2023.

Rohde, D., M. Berry, T. Do, G. O'Brien, V. Krishna, S. Varadhan, and S. Evert (2019). sparsesvd: Sparse truncated singular value decomposition (from 'SVDLIBC'), *R package version 0.2*, https://CRAN.R-project.org/package=sparsesvd (last accessed December 2022).

Shearer, P. M., R. E. Abercrombie, D. T. Trugman, and W. Wang (2019). Comparing egf methods for estimating corner frequency and stress drop from p wave spectra, *J. Geophys. Res.* **124,** no. 4, 3966–3986.

Shelly, D. R., K. Mayeda, J. Barno, K. M. Whidden, M. P. Moschetti, A. L. Llenos, J. L. Rubinstein, W. L. Yeck, P. S. Earle, R. Gök, *et al.* (2021). A big problem for small earthquakes: Benchmarking routine magnitudes and conversion relationships with coda envelope-derived mw in southern Kansas and northern Oklahoma, *Bull. Seismol. Soc. Am.* **112,** no. 1, 210–225.

Shible, H., F. Hollender, D. Bindi, P. Traversa, A. Oth, B. Edwards, P. Klin, H. Kawase, I. Grendas, R. R. Castro, *et al.* (2022). GITEC: A generalized inversion technique benchmark, *Bull. Seismol. Soc. Am.* **112,** no. 2, 850–877.

Somerville, P., and J. Yoshimura (1990). The influence of critical Moho reflections on strong ground motions recorded in San Francisco and Oakland during the 1989 Loma Prieta earthquake, *Geophys. Res. Lett.* **17,** no. 8, 1203–1206.

Thatcher, W. (1972). Regional variations of seismic source parameters in the northern Baja California area, *J. Geophys. Res.* **77,** no. 8, 1549–1565.

Wessel, P., W. H. F. Smith, R. Scharroo, J. Luis, and F. Wobbe (2013). Generic mapping tools: Improved version released, *EOS Trans. AGU* **94,** no. 45, 409–410.

Wickham, H. (2016). *ggplot2: Elegant Graphics for Data Analysis*, Springer-Verlag, New York.

Appendix

The access to source spectra and source parameters obtained in this study is described in (Bindi *et al.*, 2023). The archive is organized as a directory-tree with *duration/propagation/site/source* structure, in which the nested directories are:

- **duration**. The parent folder represents the window duration used for computing the Fourier amplitude spectra; it has names D5, D20, and Dv for the choices 5 s, 20 s, and variable duration between 5 and 20 s, respectively;
- **propagation**. It indicates the two choices made about the dependency on depth; it assumes the name HYPO and EPIH, see equations (2) and (3), respectively;
- **site**. It indicates the applied site constraint, either AVE or SEL;
- **source**. The innermost folder represents the source model selected for performing spectral fitting and extract the source parameters. As a subfolder of SEL, folder *source* can be BRUNE or BOATW, corresponding to models in equation (6) with $\gamma = 2$, $n = 1$ and $\gamma = 2$ and $n = 2$, respectively; as a subfolder of AVE, *source* has the name BRUNEK and corresponds to the model in equation (7).

An example of directory-tree is D20/HYPO/SEL/BRUNE which collects the results obtained considering 20 s windows, the attenuation model based on hypocentral distance, site amplifications constrained for a set of selected reference sites and the source spectra are fitted to the Brune model.

For the branch originated by D20, few other branching levels are available, for example:

- D20/HYPO/SEL/BOOT includes the results of the bootstrap analysis discussed in this study.
- D20/HYPO/SEL/BRUNE/APP includes the results of the apparent source spectra discussed in this study.

In terms of tables summarizing the main results, the following files are available:

- within the *propagation* folders, files named atte_"dur"_"prop".csv, in which "dur" is a tag for duration (i.e, d5, d20, or dv) and "prop" is the tag for propagation (i.e., either HYPO or EPIH). Files for HYPO include one column named *dist* reporting the hypocentral distance in km, and multiple columns reporting the spectral attenuation for different frequencies as indicated in the column name (e.g., column FAS_000.47 is listing the attenuation at 0.47 Hz); for EPIH, one additional column named *ddep* is reporting the depth value in km, and epicentral distances are reported in column *ddist*.
- within the *site* folder, files names source_"dur"_"prop"_"site".csv, in which the additional tag "site" is indicating either the site constraint SEL or AVE; these files include a column named "freq" indicating the frequency and multiple columns indicating the GIT source spectra for different events reported in the column name.
- within the *site* folder, files names siteamp_"dur"_"prop"_"site".csv, where the additional tag "site" is indicating either the site constraint SEL or AVE; these files include a column named "freq" indicating the frequency and multiple columns indicating the GIT site amplifications for different stations and channels reported in the column name.
- within the *source* folder, tables with the source parameters.

The archive also includes additional information, such as tables with event and station metadata, as well as directories with figures (e.g., source spectral fits). More details are available at Bindi *et al.* (2023).

Manuscript received 23 January 2023
Published online 23 May 2023